

Revised for J. Phys. Chem. B
on August 31, 2006

Phase Behavior of Elemental Aluminum using Monte Carlo Simulations

Divesh Bhatt, Nathan E. Schultz, Ahren W. Jasper, J. Ilja Siepmann*, Donald G. Truhlar*

*Department of Chemistry and Supercomputing Institute, University of Minnesota,
207 Pleasant Street SE, Minneapolis, MN 55455-0431*

Abstract

Monte Carlo simulations are presented for two models of aluminum, an embedded-atom model and an explicit many-body model. Vapor/liquid coexistence curves are determined using Gibbs ensemble Monte Carlo simulations. The normal boiling points predicted by both models are somewhat higher (by about 10%) than the experimental value. Isothermal constant-stress simulations are used to simulate solid Al from 300 K to the triple point. The solid structures are at least metastable in the FCC configuration, and the specific heat is determined to be lower than the experimental value. The melting point predicted for the embedded-atom model determined via thermodynamic integration along a pseudo-supercritical path is approximately 20% higher than the experimental value.

*to whom correspondence should be addressed. e-mail: siepmann@chem.umn.edu, truhlar@umn.edu

Introduction

Aluminum is of technological importance not only as a lightweight, rust-resistant structural material but also as an ingredient for high-energy fuels and, potentially, as a hydrogen storage device.¹ In many applications, e.g. the controlled growth of Al nanoparticles, precise knowledge of Al's thermodynamic properties such as the saturated vapor pressure over a large range of temperatures up to the critical point is pivotal. The high-temperature thermodynamic properties of metals in general, and Al in particular, are not known, and the present article reports computer simulations performed on analytical potential models to determine such properties. In this context, it becomes imperative that these analytical potential energy functions be validated before applying them for prediction of experimentally difficult to determine properties.

Density-functional theory (DFT)² is used quite extensively to predict potential energy functions, and the PBE0 functional³ (also called PBEh) has been shown to provide accurate potential energy functions for Al clusters.⁴ Recently, some of us and coworkers⁵ have presented analytical potential energy functions that were validated against density-functional theory (DFT) results for Al clusters and nanoparticles. At 0 K, an accurate potential function and a calculation of the zeropoint energy suffice to give a reasonably complete and accurate thermodynamic description of a cluster, nanoparticle, or solid, but at finite temperatures, the entropy is important in determining thermodynamic properties, and statistical mechanical methods must be employed.⁶ However, DFT is often prohibitively costly for use in finite-temperature

statistical mechanical simulations,⁷ and analytic potential models become useful. Accordingly, phase equilibrium calculations on bulk systems with known thermodynamic properties provide an additional and important way to further validate the analytic potential energy functions, which can then be used to calculate bulk properties under conditions where they are not well known experimentally⁸ as well as calculating finite-temperature properties of large clusters and nanoparticles that have been recalcitrant to experimental size-selected measurement.

Thus, the main aim of this manuscript is to test the applicability of two analytical potential energy functions for Al, previously validated against DFT results at 0 K, against known experimental results such as the normal boiling point and melting point. Previously, we calculated the vapor–liquid coexistence properties of two embedded-atom potential energy functions and highlighted the sensitivity of the phase diagram to the force field parametrization.⁸ While an embedded-atom potential fitted to solid state data⁹ yields an unsatisfactory description of the vapor-liquid coexistence curve (VLCC), another potential function fitted to clusters and nanoparticles of various sizes¹⁰ gives an accurate description of the VLCC at lower temperatures (where experimental data are available) and allows for the prediction of Al’s critical point.⁸

This manuscript is organized as follows. First, the potential models that are used for aluminum are described. Then, the details of the simulation methodologies used to simulate various thermodynamic properties of Al are given. This is followed by results and detailed discussions of the vapor–liquid equilibria, simulations of solid

Al structures, the solid–vapor equilibria, and the melting point. The final section summarizes the key conclusions.

Potential Models for Aluminum

We explore two different potential models for Al. The first is an example of an embedded-atom (EAM) model.¹¹ The total energy of a system of N atoms interacting via an EAM potential is given by^{5,9–11}

$$U = \sum_i^N F(\rho_i) + \sum_{i>j} \phi(r_{ij}) \quad (1)$$

and where r_{ij} is the distance between two atoms i and j , and the first term in eq 1 (the embedding energy) is model dependent. For the EAM model employed by Mei and Davenport⁹, this function is given by

$$F(\rho) = -E_c \left[1 - \frac{\alpha}{\beta} \ln \left(\frac{\rho}{\rho_e} \right) \right] \left(\frac{\rho}{\rho_e} \right)^{\alpha/\beta} + \frac{1}{2} \phi_0 \sum_{m=1}^3 s_m \exp [-(\sqrt{m} - 1)\gamma] \\ \times \left[1 + (\sqrt{m} - 1)\delta - \sqrt{m} \frac{\delta}{\beta} \ln \left(\frac{\rho}{\rho_e} \right) \right] \left(\frac{\rho}{\rho_e} \right)^{\sqrt{m}\gamma/\beta} \quad (2)$$

with

$$\rho_i = \sum_{j(\neq i)} \Delta(r_{ij}) f(r_{ij}), \quad (3)$$

$$f(r_{ij}) = \rho_e \sum_{l=0}^5 \frac{c_l}{12} \left(\frac{r_0}{r_{ij}} \right)^l, \quad (4)$$

and

$$\Delta(r) = \begin{cases} 1 & r \leq r_n \\ (1-x)^3(1+3x+6x^2) & r_n < r < r_c \\ 0 & r \geq r_c \end{cases} \quad (5)$$

where $x = (r - r_n)/(r_c - r_n)$. The second term in eq 1 is a pairwise interaction given by

$$\phi(r) = -\phi_0 \left[1 + \delta \left(\frac{r}{r_0} - 1 \right) \right] \exp \left[-\gamma \left(\frac{r}{r_0} - 1 \right) \right]. \quad (6)$$

The parameters used in eqs 1–6 are given in Table 1. Many-body interactions appear in this potential in the density-dependent term, $F(\rho)$, although all terms are functions of the set of pairwise additive distances. Thus, the potential is a function of interpair distances but is not pairwise additive. This form of the EAM potential was used by Mei and Davenport,⁹ with different parameters than those given in Table 1, to calculate the melting point of Al as 800 ± 9 K. Recently, Jasper *et. al.*⁵ have reparametrized the EAM potential for a large data set of Al cluster and nanoparticle energies. Table 1 represents the result of this reparametrization, which is called NP-B in Ref 5, but is simply called EAM here.

The second Al potential that is considered in this work is an explicit many-body potential (EMB), also parametrized in Ref 5, where it is called NP-A. The form of this potential is given by⁵

$$U = \sum_{i>j} u_2(r_{ij}) - \sum_{i>j} u'_2(r_{ij}) [f_{ij}^S + f_{ij}^{CN}] \quad (7)$$

where the explicit pair potentials, u_2 and u'_2 , are given by

$$u_2(r_{ij}) = -D_e(1 + a_1 Y_{ij} + a_2 Y_{ij}^2 + a_3 Y_{ij}^3) \exp(-a_1 Y_{ij}) \quad (8)$$

and

$$u'_2(r_{ij}) = -D'_e(1 + a'_1 Y'_{ij} + a'_2 Y'^2_{ij} + a'_3 Y'^3_{ij}) \exp(-a'_1 Y'_{ij}) \quad (9)$$

where $Y_{ij} = r_{ij} - r_e$ and $Y'_{ij} = r_{ij} - r'_e$. Explicit multi-body terms appear through the screening function, f_{ij}^S , and the coordination number function, f_{ij}^{CN} . The screening function is

$$f_{ij}^S = \tanh(\chi_{ij}^S) \quad (10)$$

where

$$\chi_{ij}^S = \kappa_1 \sum_{k \neq i, j} \exp[-\kappa_2 (r_{ik} + r_{jk})^{\kappa_3} / r_{ij}^{\kappa_3}] \quad (11)$$

The coordination number function is

$$f_{ij}^{\text{CN}} = d(1 - G_{ij}) \quad (12)$$

where

$$G_{ij} = \frac{1}{1 + \left(\frac{g_i - f_g(r_{ij})}{g_0}\right)^\gamma} \frac{1}{1 + \left(\frac{g_j - f_g(r_{ij})}{g_0}\right)^\gamma}, \quad (13)$$

g_i is the effective coordination number of atom i defined by

$$g_i = \sum_{k \neq i} f_g(r_{ik}), \quad (14)$$

and the weighting function, f_g is

$$f_g(r_{ij}) = \begin{cases} \exp\left(\gamma_1 + \frac{\gamma_1 \gamma_2}{r_{ij} - \gamma_2}\right) & \text{if } r_{ij} < \gamma_2 \\ 0 & \text{if } r_{ij} \geq \gamma_2 \end{cases}. \quad (15)$$

The parameters⁵ of eqs 7–15 are given in Table 2. We note that the parameters for u_2 were adjusted to fit data for Al_2 and a large data set including Al_N clusters and nanoparticles with $N = 3 - 177$ was then used to optimize the parameters for u'_2 , f^S , and f^{CN} .⁵ The many-body terms were designed to vanish at large separations, giving

the EMB potential the correct two-body limit. Thus, the EMB potential reproduces the dimer binding energy very well with an error of only 0.01 eV.⁵ In contrast, the EAM potential which was fully optimized over the entire data set, including the dimer data, overbinds Al₂ by 0.38 eV.⁵ Nevertheless, the fitting errors measured over the entire data set are similar for the EAM and EMB models (0.05 eV/atom and 0.03 eV/atom, respectively).

Simulation Methods

Vapor-liquid coexistence. The vapor-liquid coexistence curve is determined using Gibbs-ensemble Monte Carlo (GEMC) simulations,^{12,13} employing translations, aggregation-volume-bias Monte Carlo¹⁴ moves to sample clustering in the vapor phase, volume exchanges, and configuration-bias Monte Carlo swaps.^{15,16} For the EAM potential, 350 Al atoms with periodic boundary conditions are employed. The size of the vapor box is adjusted such that about 50 atoms are in the vapor phase. Since a liquid structure is used as the initial configuration, these GEMC can be extended to temperatures below the triple point, i.e. into a region where the liquid phase is only metastable compared to the solid phase.¹⁷ Averages are collected for 100,000 cycles after allowing 50,000 equilibration cycles. Each cycle consists of N moves (where N is the total number of atoms in the simulation boxes of the Gibbs ensemble). Evaluation of the EAM potential scales as N^2 , whereas that for the EMB potential scales as N^3 ; thus a smaller system size was used for the EMB calculations. For the EMB model, the simulation includes 150 atoms, of which about 20 atoms are in the vapor phase. For the EMB potential, 40,000 equilibration cycles are followed by 40,000 production

cycles during which the averages are collected. For the EAM potential, additional GEMC simulations were performed at the two highest temperatures for a system of 800 Al atoms. As noted in our previous work,⁸ the effect of increasing the box size on the vapor-liquid coexistence properties calculated with the EAM potential was negligible; due to its more expensive nature, such a study was not conducted for the EMB potential.

Periodic solid structures. Isothermal constant-stress Monte Carlo simulations¹⁸ are used to explore the FCC solid for both potentials. In these simulations, Monte Carlo moves allow for sampling of the cell parameters (*i.e.*, the three lengths and three angles that describe the periodic simulation cell) in accordance to a constant external stress, as first suggested by Parrinello and Rahman for molecular dynamics simulations.^{19,20} The initial starting structure is FCC, which has the lowest lattice energy, and the non-cubic primitive cell was replicated to yield simulation boxes of a suitable size. For the EAM potential, 392 atoms are in the simulation cell and 60,000 cycles are used; whereas 252 atoms are simulated for 60,000 cycles for the EMB potential.

Solid-vapor coexistence. To determine the solid/vapor coexistence for Al, we chose the starting structures to be the equilibrated constant-stress structures generated above. The solid-slab GEMC method of Chen *et al.*¹⁷ was employed. Thus, a vapor space (of the thickness of the solid slab) was added to the exposed 111 surface of a solid slab on either side (thus, tripling the length of the box containing the solid slab). Due to the addition of the vapor space, the exchange of atoms between the

solid structure and the second vapor box of the Gibbs-ensemble is greatly facilitated by allowing the exchange to occur from the surface of the solid slab.¹⁷ The size of the vapor box is chosen such that about 10-15% of the atoms are in the vapor box.

Melting point. To determine the melting point, thermodynamic integration²¹ along a pseudo-supercritical path is performed. In this method,^{22,23} the average volumes of the two bulk phases (V_{liq} and V_{sol} , in the case of melting) are determined using isothermal-isobaric simulations at the melting pressure of interest (usually 1 atm) and a temperature at which both phases are (meta)stable. Subsequently, the Helmholtz free energy difference between the two phases at their average volumes is calculated via thermodynamic integration along a pseudo-supercritical path. This path is divided into three distinct stages. Only a brief description is given here, further details are available elsewhere 22 and 23. In stage A, the liquid is transformed into a weakly attracting fluid at a system volume V_{liq} . Accordingly, a series of canonical ensemble simulations are performed in which the strength of intermolecular interactions is gradually scaled down. In stage B, the intermolecular interactions are kept at their scaled-down values, and an external potential that acts at the lattice sites of an ordered solid is gradually turned on. The form of this external potential is Gaussian (ae^{-br^2} ; as in the original references, with $a = 3.45$ eV and $b = 0.76 \text{ \AA}^2$; the values of a and b are somewhat arbitrary, but result in gradual ordering of the atoms into a lattice as the external potential is turned on). Additionally, the volume is also changed from V_{liq} to V_{sol} in this stage. In the final stage C, the external potential is gradually turned off, and the full intermolecular potential is gradually restored.

Thus, at the end of stage C, a regular bulk solid phase is obtained. The Gibbs free energy difference between the the liquid and the solid phase at the particular state point (given by T and p) is obtained as

$$\Delta G(T, p) \equiv G_{\text{liq}} - G_{\text{sol}} = \Delta F_{\text{A}}^{\text{ex}} + \Delta F_{\text{B}}^{\text{ex}} + \Delta F_{\text{C}}^{\text{ex}} + \Delta F^{\text{id}} + p(V_{\text{liq}} - V_{\text{sol}}) \quad (16)$$

where F_i^{ex} is the difference in excess Helmholtz free energies at the beginning and the end of stage i calculated from thermodynamic integration, and F^{id} is the ideal part that is calculated analytically (and equals $RT \ln(\rho_{\text{s}}/\rho_{\text{l}})$, where ρ_{s} is the density of the solid at the given T and p , and ρ_{l} is the liquid density under the same conditions).

A system size of 256 atoms with periodic boundary conditions was used. In addition to the liquid box, the solid box is also cubic with an FCC structure. For each stage, thermodynamic integration is performed using 20–30 points (with a higher point density in the region where the integrand is rapidly varying). Once the Gibbs free energy difference is calculated at a given T and p , it is evaluated at other T using multiple-histogram reweighting²⁴ for each bulk phase.

Results and Discussion

Vapor liquid equilibria. The vapor-liquid coexistence curve (VLCC) for the EAM potential is obtained for a temperature range from 1100 to 5250 K. At lower temperatures, the particle exchange moves are very inefficient. For the EMB potential, the VLCC is investigated between 1200 and 5500 K. Figure 1 shows the temperature-density phase diagram for liquid–vapor coexistence with diamonds for the EAM potential and circles for the EMB potential. The open symbols represent

the GEMC results, whereas the filled ones are the critical points obtained by the method discussed next.

As noted in our previous work, two different methods are used to obtain the critical properties. In the first method, the critical temperature is obtained from the scaling law²¹

$$\rho_l - \rho_v \sim (T_c - T)^\beta \quad (17)$$

where ρ_l and ρ_v are the liquid and vapor coexistence densities, respectively, T_c is the critical temperature, and the scaling coefficient β is the critical exponent²⁵ with a value of 0.325. Additionally, the critical density ρ_c is obtained from the law of rectilinear diameters²¹

$$\frac{\rho_l + \rho_v}{2} = \rho_c + A(T - T_c) \quad (18)$$

where A is a slope obtained by fitting. The second method uses additional terms in the scaling and rectilinear laws to account for deviations from corresponding states.³⁰

As in our previous work,⁸ simulated temperatures above the normal boiling point were used in the fits to obtain the critical properties. The average value of the critical temperature for the EAM potential from the two methods is 6299 ± 48 K, and the critical density is 707 ± 60 kg/m³. Critical properties for the EMB potential are obtained, in the manner described above, as $T_c = 7075 \pm 45$ K and $\rho_c = 538 \pm 8$ kg/m³. As compared to the VLCC of the EAM potential, the VLCC of the EMB potential shows a lower saturated liquid density at low and intermediate temperatures, but the curves cross at about 5500 K. Moreover, the vapor coexistence densities are higher for the EAM potential. This results in a higher T_c for the EMB potential.

The normal (*i.e.*, 1 atm) boiling temperature, T_b , is usually obtained from the the simulations using the Clausius-Clapeyron equation^{31,32}

$$\frac{d \ln p_v}{d(1/T)} = -\frac{\Delta H_{lv}}{R} \quad (19)$$

where p_v is the vapor pressure ($= \rho_v RT$), and ΔH_{lv} is the heat of vaporization. However, the form of the EAM potential does not permit a straightforward calculation of the pressure via the virial route^{??} because although the force on a given atom can be computed, this force cannot be decomposed simply into pairwise additive terms. To overcome this problem, an alternate method that utilizes the thermodynamic definition of pressure is used,²⁶

$$p = p_{id} - \left\langle \frac{\partial U}{\partial V} \right\rangle \quad (20)$$

where p_{id} is the ideal-gas contribution to the pressure, U is the potential energy of the system, and the averaging is done in a system with fixed volume (such as a canonical ensemble). Accordingly, additional NVT simulations are performed at the average GEMC vapor densities, and the pressure is calculated using eq 20. For a given configuration in the canonical ensemble simulations, $\partial U/\partial V$ is calculated by performing small test volume changes.²⁶

The resulting plot of p_v as a function of $1/T$ for four values of vapor pressure closest to 1 atm is shown in Figure 2 for both the potentials. The experimental data is depicted by the solid line. The temperature corresponding to $p_v = 1$ atm gives $T_b = 2993 \pm 8$ K. Compared to the experimental normal boiling point of 2792 K,²⁷ the EAM potential overestimates T_b for Al by about 7%. For the EMB potential, a

similar procedure yields T_b to be 3097 ± 9 K. Thus, compared to the more expensive EMB potential, the EAM potential gives a slightly better estimate of the normal boiling point. However, a reliable value of the experimental T_c is unavailable⁸ to make similar comparison of the two Al potentials for a wider range of the vapor-liquid coexistence.

Constant-stress simulations. Constant-stress simulations for the face-centered cubic (FCC) solid are performed at 1 atm and several different temperatures for the EAM potential. Although the experimental melting point of Al is 933.5 K,²⁷ the structures are at least metastable as crystalline solids up to at least 1250 K. Figure 3 depicts the orientational order parameter, Q_6 ,^{28,29} as a function of the number of MC cycles for 900 K, 1250 K, and 1300 K. In calculating Q_6 , the neighbors as defined as pairs of atoms that are closer than the first minimum in the radial distribution functions. For a crystalline solid, Q_6 is approximately 0.5, and it approaches a value of 0 in the thermodynamic limit for a homogeneous liquid.²⁹ From the values of Q_6 in Figure 3, it is clear that the structures remain crystalline at 900 and 1250 K. On the other hand, as the simulation proceeds at 1300 K, the starting structure loses its crystallinity. For comparison, instantaneous density profiles (after 60,000 cycles) for the EAM potential are shown for 1300 K, 1250 K, and 900 K in Figure 4. These density profiles are collected in bins of width 0.25 Å. In each figure, z is the direction perpendicular to the 111 plane. Thus, the spikes in the density profiles at 900 K (panel (c)) and 1250 K (panel (b)) indicate a solid-like structure with the atoms on sets of parallel 111 planes. The spacing between the spikes is approximately 2.8 Å,

corresponding to the lattice spacing between adjacent Al atoms. Upon increasing the temperature to 1250 K, the density spikes broaden, as expected. However, at 1300 K, the density profile indicates the onset of melting.

For 900 K, the layered structure is shown in more detail in Figure 5; the ABC stacking representative of the an FCC lattice can be clearly seen. This FCC stacking is maintained for all the solid structures. It should be pointed out that the preservation of the FCC structure does not imply that the FCC structure is the most stable one. It does indicate, however, that the FCC structure is probably at least metastable.

Table 3 shows the densities and enthalpies of the solid structures as functions of temperature. At 300 K, the density of EAM Al is almost identical to the experimental density of aluminum (at 293 K, the experimental density is 2.699^{27} g/cm³). Also, since all the simulations are performed at 1 atm, the specific heat, $C_p = (\delta H/\delta T)_p$ can be evaluated. The filled circles of Figure 6 depict the enthalpies as a function of temperature. Given the wide range of T simulated, it is unlikely that C_p can be approximated as a constant; this is confirmed by the nonlinearity of the enthalpy-temperature plot in Figure 6. However, the enthalpy can be well approximated by a quadratic fit, and, as expected, the specific heat is an increasing function of temperature. From a quadratic fit to the data, the specific heat is estimated to be 15.2 ± 0.4 J/mol K at 300 K and 19.6 ± 0.6 J/mol K at 900 K. Compared to the experimental values²⁷ of 24.2 and 32.6 J/mol K at 300 and 900 K, respectively, the heat capacity for the EAM potential is smaller by about 40% at both temperatures.

For the EMB potential, one constant-stress simulation at 1000 K was performed.

As also observed for the EAM potential, the FCC structure for the EMB potential is at least metastable at 1000 K and has an enthalpy of -315.2 kJ/mol. This is larger by about 1 kJ/mol than the enthalpy value for the EAM potential at 1000 K. The reverse is observed for the enthalpies of the liquid phases for the EMB and EAM potentials at 1200 K.

Solid-vapor equilibria. As outlined earlier, the solid structures generated along the 111 surface are surrounded by vapor, and solid-slab GEMC simulations are performed to calculate the solid/vapor coexistence. At lower T (below 950 K) there are a few to no particle exchange moves between the solid slab and the vapor boxes. The orientational order parameter, Q_6 , is shown as a function of the number of MC cycles for two different temperatures in Figure 7. At 1075 K, the value of Q_6 shows that the system is a crystalline solid throughout the entire length of the simulation. In contrast, the structure at 1100 K melts, resulting in a lower value of Q_6 . Since the current system is in solid/vapor equilibrium, the pressure on the solid structure is the vapor pressure of EAM Al at that temperature, in contrast to the above constant-stress simulations at 1 atm. However, for this range of pressure, the solid structure is still FCC at 1075 K, as can be seen in Figure 8 where the atoms in three adjacent layers are shown by different symbols (similar to Figure 5).

The temperature at which the solid slab melts, *i.e.*, 1100 K, can be contrasted with the temperature of 1250 K mentioned above for which the periodic solid structures (without solid/vapor interface in the simulation box) are at least metastable. The presence of a solid/vapor interface allows for surface melting to occur and the free

energy barrier from the solid to the liquid phase is greatly lowered.

Figure 9 shows the Clausius-Clapeyron plot for the solid–vapor coexistence as closed symbols and the dashed line represents the best fit. On the same graph, the open circles denote the vapor–liquid coexistence results obtained above. Because of the very low coexistence vapor density, the vapor pressure for the solid–vapor coexistence at a given T is obtained by treating the vapor phase as an ideal gas instead of performing additional NVT simulation at average vapor density (as in the case of vapor/liquid coexistence). The triple point can, in principle, be determined from the intersection of the sublimation and the boiling vapor pressure lines on such a plot. However, the slopes of the Clausius-Clapeyron plot for the solid-vapor coexistence are almost identical to the slope of the liquid-vapor coexistence. This prevents an accurate determination of the triple point for the EAM potential using this method. An additional issue that arises in such solid-slab simulations is whether the slab is thick enough to allow for an interior region with bulk properties because surface relaxation and melting can be observed for slabs.¹⁷ Effects of the slab thickness were not explored in this work because of the very small heat of fusion. Thus, as described in the following section, the melting point is obtained using a different route.

Melting Point. Isobaric-isothermal ensemble simulations at 1100 K and 1 atm with the EAM potential yield a box length of 16.823 Å for the cubic liquid box containing 256 atoms, and a length of 16.553 Å for the cubic FCC solid box with 256 atoms. Using these two volumes for the bulk condensed phases, explicit thermodynamic integration is performed at 1100 K yielding $\Delta F_A^{\text{ex}} = 256.26 \pm 0.02$ kJ/mol,

$\Delta F_B^{\text{ex}} = -294.09 \pm 0.05$ kJ/mol, and $\Delta F_C^{\text{ex}} = 37.21 \pm 0.04$ kJ/mol. The error in these values are due to uncertainties in the values of the integrand at each integration point, and do not represent the errors due to the discrete nature of the integration itself. Using these values in eq 16, we find that $\Delta G(1100 \text{ K}, 1 \text{ atm}) = 0.19 \pm 0.11$ kJ/mol. Accordingly, the solid phase is more stable than the liquid phase at 1100 K and 1 atm, and the normal melting point of EAM Al is higher than 1100 K.

Multiple histogram reweighting simulations in the isobaric-isothermal ensemble for each bulk phase were performed at 4 different temperatures (1080, 1100, 1120, and 1140 K) and 1 atm. Figure 10 shows the Gibbs free energies (relative to the respective values at 1100 K) for both the solid and the liquid phases. It must be noted here that the reference values for free energies for the two phases are different, and the purpose of Figure 10 is to highlight that the free energy of the solid phase decreases more rapidly than that of the liquid phase. Combining Figure 10 with the value of $\Delta G(1100 \text{ K}, 1 \text{ atm})$ given above, yields Figure 11, which depicts the difference in Gibbs free energies of liquid and the solid phase as a function of T . The figure shows that $\Delta G(T, 1 \text{ atm})$ changes sign at 1122 K. Thus, the normal melting point of EAM Al is 1122 ± 13 K, where the error bar is based on the uncertainty of $\Delta G(1100 \text{ K}, 1 \text{ atm})$. This is higher than the experimental value of 933 K by approximately 20%.

For the more expensive EMB potential, explicit thermodynamic integration is not performed to determine the melting point. However, the similarities of the enthalpies for the solid and liquid phases at 1000 and 1200 K, respectively, obtained for the EMB

and EAM potentials (see above) give an indication that the EMB potential would lead to a similar overestimation of the melting point.

The effect of pressure on the melting point was studied by a similar procedure for two different pressures. In one case, explicit thermodynamic integration, performed at 1000 K and 5.9×10^{-10} atm (vapor pressure of the liquid at 1100 K, as obtained from GEMC simulations), yields ΔG to be 1.17 ± 0.12 kJ/mol. In combination with multiple histogram reweighting (at 1000 K, 1040 K, 1070 K, 1100 K, and 1140 K and at the given pressure) the melting point at the above stated pressure is obtained as 1132 ± 15 K. This value is statistically the same as that at 1 atm. In the second case, explicit thermodynamic integration is performed at 1100 K and at 10000 atm; ΔG is then calculated to be 0.99 ± 0.10 kJ/mol. Multiple histograms at 1050 K, 1100 K, 1150 K, and 1200 K result in a melting point of 1215 ± 13 K. Accordingly, an increase in pressure to values encountered inside Earth's crust leads to a significant increase in the melting point.

Vocadlo and Alfe³³ and Alfe *et al.*³⁴ calculated the melting curve of Al for pressures (up to 150 GPa) using *ab initio* molecular dynamics simulations. They calculated the liquid-phase free energy by constructing a thermodynamic reversible path to a Lennard-Jones fluid (and subsequently using the Lennard-Jones equation of state of Johnson *et al.*³⁵). The free energy of the solid was computed by referencing to a harmonic crystal. As in the current work, a significant increase in melting point was observed with an increase in pressure.^{33,34} Further, the slope of the melting curve was calculated to be approximately 80 K/GPa,³³ a value that agrees well with the current

work (an increase in the melting point of approximately 100 K with an increase in pressure by ~ 1 GPa).

The form of the EAM potential for Al is same as the original Mei-Davenport embedded-atom (MDEAM) potential⁹ for Al that is parametrized to bulk solid-state data. Thus a comparison of the results obtained with EAM potential to those obtained with their original parameters (called the MDEAM potential) is helpful in determining the effect for parameterizing potentials not only to match bulk solid-state data but also to reproduce accurate energies of clusters and nanoparticles of various sizes (from dimer to bulk). Mei and Davenport calculated a value of 800 K for the melting point of the MDEAM potential; this underestimates the experimental value by 14%, whereas the present value of 1122 K is a 21% overestimate. In a previous study, we reported that the MDEAM potential dramatically underestimates both the boiling point and the heat of vaporization.⁸

Conclusions

The thermodynamic properties of Al are calculated for two nonpairwise-additive potentials. Vapor-liquid equilibria are determined using Gibbs-ensemble Monte Carlo. The more expensive EMB potential shows a lower saturated vapor density than the EAM potential for a wide range of temperatures. Accordingly, the critical temperature of the EMB potential is higher than that of the EAM potential. From the vapor pressures, the normal boiling point is determined for both the potentials. In accord with the higher value of the critical temperature, the normal boiling point of the EMB potential is higher than that for the EAM potential. In turn, both the

potentials overestimate the experimental normal boiling point.

Constant-stress simulations in the solid phase show that the FCC structure remains stable over a range of temperatures and that the density of Al at ambient conditions using the EAM potential is very close to the experimental value. The specific heat of the solid phase increases with the temperature, and is lower than the experimental value. Solid-slab Gibbs ensemble simulations are performed to determine the solid-vapor coexistence of the EAM potential. For this purpose, the 111 facet of the FCC structure is exposed to the vapor phase. Compared to a periodic solid (without any vapor phase surrounding it) of the constant-stress simulations, surface melting results in a significantly lower melting temperature. However, an accurate determination of the triple point using the vapor pressure *versus* temperature plot is precluded by almost identical enthalpies of vaporization and of sublimation. Thermodynamic integration along a pseudo-supercritical path gives a value of the melting point of EAM Al as 1122 K that is approximately 20% higher than the experimental value.

This study highlights the efficacy of analytical potentials parametrized to reproduce accurate DFT energies for clusters of various sizes⁵ in making useful predictions of bulk thermodynamic phase behavior. While an earlier embedded-atom model by Mei and Davenport⁹ yields very inaccurate results for dimers and smaller clusters that results in a significant error for the vapor–liquid coexistence curve due to formation of dimers in the vapor phase⁸, the present EAM potential yields significantly improved binding energies for smaller clusters, a small fraction of aggregates in the saturated

vapor phase, and hence, a fairly accurate heat of vaporization and boiling point. The more expensive EMB potential yields similar results for the vapor–liquid coexistence curve, but its functional form is more physical, and it performs better than EAM for small clusters.

This work was supported in part by the Defence-University Research Institute in Nanotechnology (DURINT) of the U.S. Army Research Office under agreement number DAAD190110503 and by the National Science Foundation under grants CTS-0553911, CHE-0349122, and ITR-0428774 (VLab). A Research Scholar Award for D.B. from the Minnesota Supercomputing Institute is gratefully acknowledged.

References

1. Zuttel, A.; Wenger, P.; Sudan, P.; Mauron, P.; Orimo, S. *Mat. Sci. Eng.* **2004**, *B108*, 9.
2. Kohn, W. *Rev. Mod. Phys.* **1999**, *71*, 1253.
3. Adamo, C.; Barone, V. *J. Chem. Phys.* **1999**, *110*, 6158.
4. Schultz, N. E.; Staszewska, G.; Staszewska, P.; Truhlar, D. G. *J. Phys. Chem. B* **2004**, *108*, 4850.
5. Jasper, A. W.; Schultz, N. E.; Truhlar, D. G. *J. Phys. Chem. B* **2005**, *109*, 3915.
6. Hill, J.-R.; Subramanian, L.; Maiti, A. *Molecular Modeling Techniques in Material Science* (CRC Press, Boca Raton, 2005).
7. McGrath, M. J.; Siepmann, J. I.; Kuo, I.-F. W.; Mundy, C. J.; VandeVondele, J.; Hutter, J.; Mohamed, F.; Krack, M. *J. Phys. Chem. A* **2006**, *110*, 646.
8. Bhatt, D.; Jasper, A. W.; Schultz, N. E.; Siepmann, J. I.; Truhlar, D. G. *J. Am. Chem. Soc.* **2006**, *128*, 4224.
9. Mei, J.; Davenport, J. W. *Phys. Rev. B* **1992**, *46*, 21.
10. Jasper, A. W.; Staszewski, P.; Staszewska, G.; Schultz, N. E.; Truhlar, D. G. *J. Phys. Chem. B.* **2004**, *108*, 8996.

11. Daw, M. S.; Baskes, M. I. *Phys. Rev. Lett.* **1983**, *85*, 1285.
12. Panagiotopoulos, A. Z. *Mol. Phys.* **1987**, *61*, 813.
13. Panagiotopoulos, A. Z.; Quirke, N.; Stapleton, M.; Tildesley, D. J. *Mol. Phys.* **1988**, *63*, 527.
14. Chen, B.; Siepmann, J. I. *J. Phys. Chem. B* **2000**, *104*, 8725.
15. Siepmann, J. I.; Frenkel, D. *Mol. Phys.* **1992**, *75*, 59.
16. Mooij, G. C. A. M.; Frenkel, D.; Smit, B. *J. Phys.: Cond. Mat.* **1992**, *4*, L255.
17. Chen, B.; Siepmann, J. I.; Klein, M. L. *J. Phys. Chem. B* **2001**, *105*, 9840.
18. Najafabadi, R.; Yip, S. *Scripta Metall.* **1983**, *17*, 1199.
19. Parrinello, M.; Rahman, A. *Phys. Rev. Lett.* **1980**, *45*, 1196.
20. Parrinello, M.; Rahman, A. *J. Appl. Phys.* **1981**, *52*, 7182.
21. Frenkel, D.; Smit, B. *Understanding Molecular Simulations*: Academic Press, 1991.
22. Grochola, G. *J. Chem. Phys.* **2004**, *120*, 2122.
23. Eike, D. M.; Brennecke, J. F.; Maginn, E. J. *J. Chem. Phys.* **2005**, *122*, 014115.
24. Ferrenberg, A. M.; Swendsen, R. H. *Phys. Rev. Lett.* **1988**, *61*, 2635.
25. Rowlinson, J. S.; Widom, B. *Molecular Theory of Capillarity*: Clarendon Press, Oxford, 1982.

26. Hummer, G.; Jensen, N. G.; Neumann, M. *J. Chem. Phys.* **1998**, *109* 2791.
27. *CRC Handbook of Chemistry and Physics*, 85th Ed., (CRC Press, Boca Raton, 2004, Section 4).
28. Steinhardt, P. J.; Nelson, D. R.; Ronchetti, M. *Phys. Rev. B* **1983**, *28*, 784.
29. van Duijneveldt, J. S.; Frenkel, D. *J. Chem. Phys.* **1992**, *96*, 4655.
30. Sengers, J. V.; Level-Sengers, J. M. H. In *Progress in Liquid Physics* Croxton, C. A., Ed. (Wiley: Chichester, 1978); pp. 103-174.
31. R. Clausius, *Poggendorff's Annalen der Physik und Chemie* **1850**, *79*, 368.
32. Smith, J. M.; Van Ness, H. C. *Introduction to Chemical Engineering Thermodynamics*: (McGraw-Hill International Edition, 1987, Chapter 6).
33. Vocadlo, L.; Alfe, D. *Phys. Rev. B* **2002**, *65*, 214105.
34. Alfe, D.; Vocadlo, L.; Price, G. D.; Gillan, M. J. *J. Phys.: Cond. Matt.* **2004**, *16*, S973.
35. Johnson, K.; Zollweg, J. A.; Gubbins, K. E.; *Mol. Phys.* **1993**, *78*, 591.

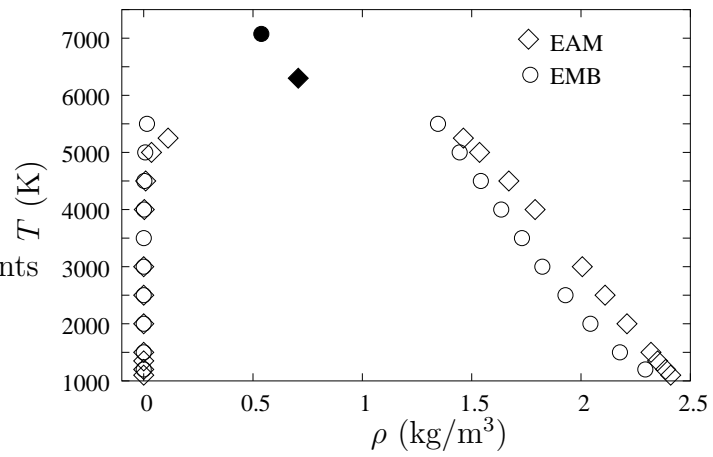


Figure 1: Vapor-liquid coexistence curves for the EAM (diamonds) and EMB (circles) potentials. The corresponding closed symbols represent the respective critical points.

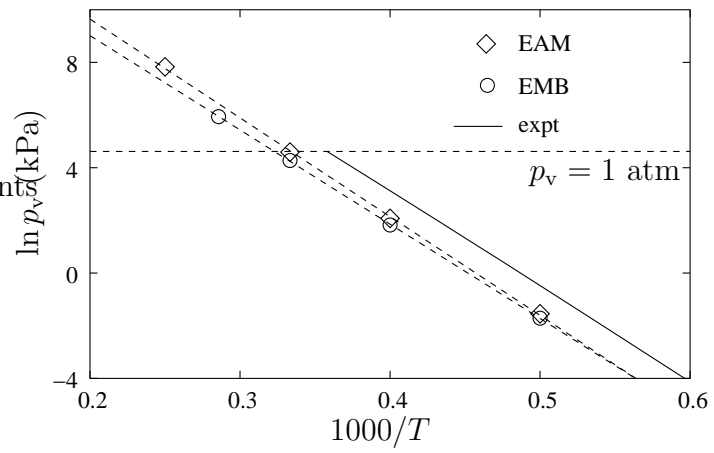


Figure 2: Clausius-Clapeyron plot for the EAM and the EMB potentials. The dashed line through each set is a least squares fit.

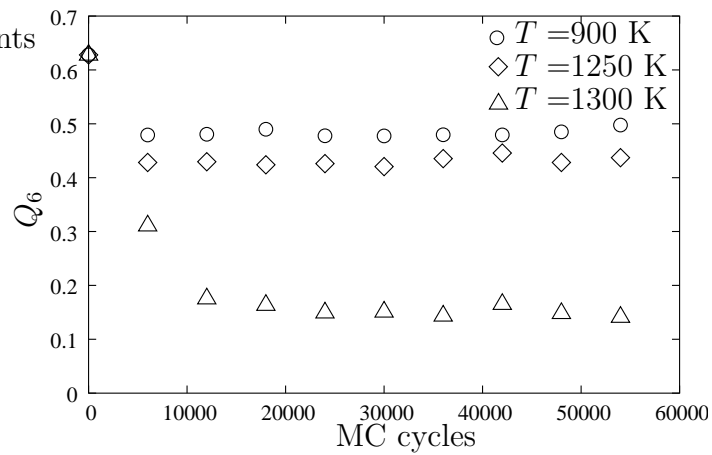


Figure 3: Instantaneous orientational order parameter as a function of MC cycles for bulk structures at three different temperatures obtained from constant-stress simulations at 1 atm. All simulations were started from the fcc structure.

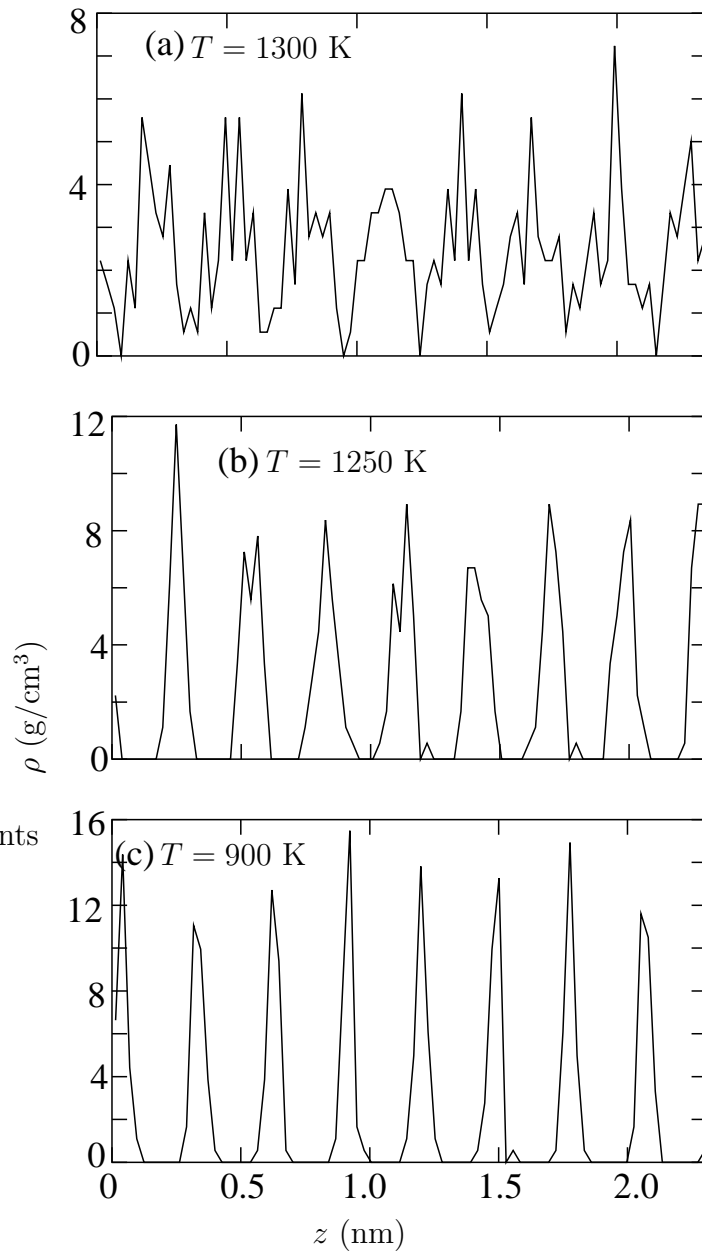


Figure 4: Bulk density profiles along the direction perpendicular to the 111 plane obtained from constant-stress simulations for the EAM Al potential at a pressure of 1 atm and three different temperatures.

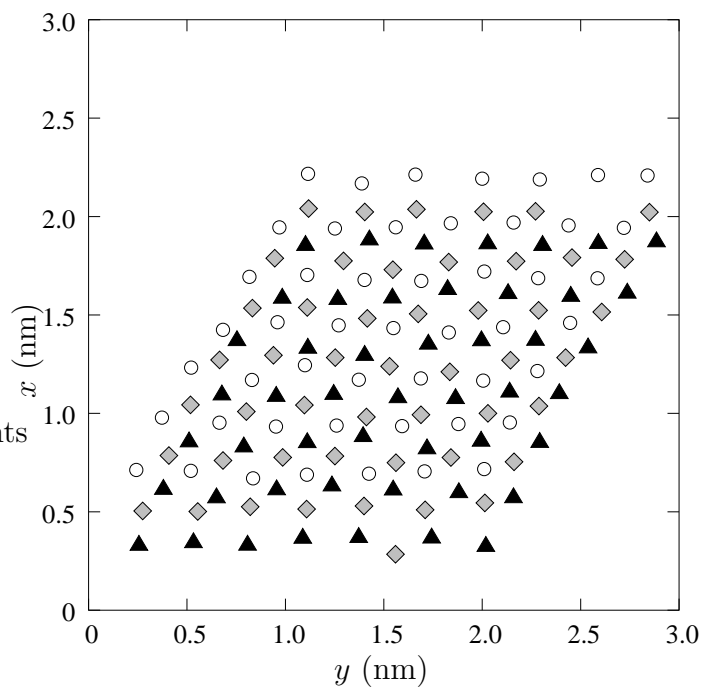


Figure 5: Stacking of the atoms in three adjacent 111 planes at 900 K obtained from the constant-stress simulations for bulk periodic systems. The open circles represent the first layer, the gray diamonds are in the second layer, and the black triangles are in the third layer.

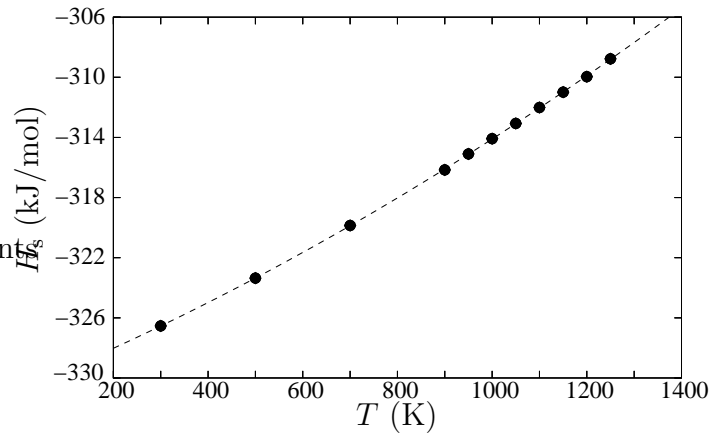


Figure 6: Enthalpy of the bulk fcc solid as a function of temperature for the EAM potential at 1 atm. A quadratic fit is shown by the dashed line with $H_s = -330.8 + 0.0130T + 3.644 \times 10^{-6}T^2$.

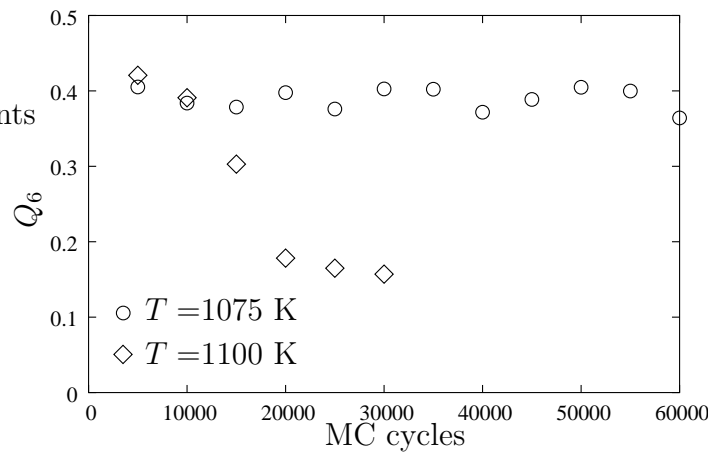


Figure 7: Instantaneous orientational order parameter as a function of MC cycles for structures at two different temperatures obtained from solid-slab simulations.

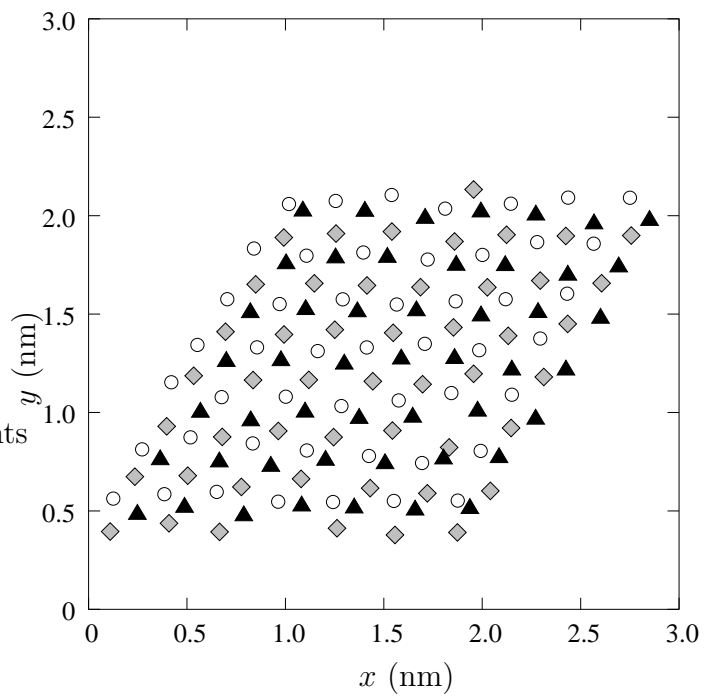


Figure 8: Stacking of the atoms on on three adjacent 111 planes at 1075 K for the solid-slab simulation. Symbols as in Figure 5.

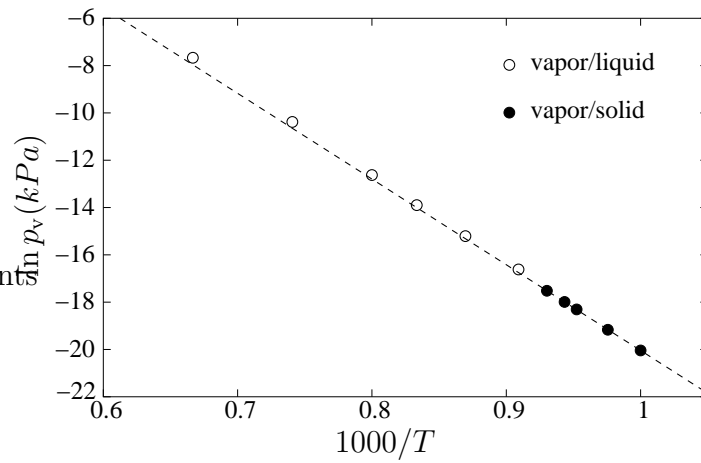


Figure 9: Clausius-Clapeyron plot for the solid-vapor coexistence for the EAM potential represented by the closed circles. The dashed line is the best fit to the sublimation pressure and the open circles are the liquid-vapor data.

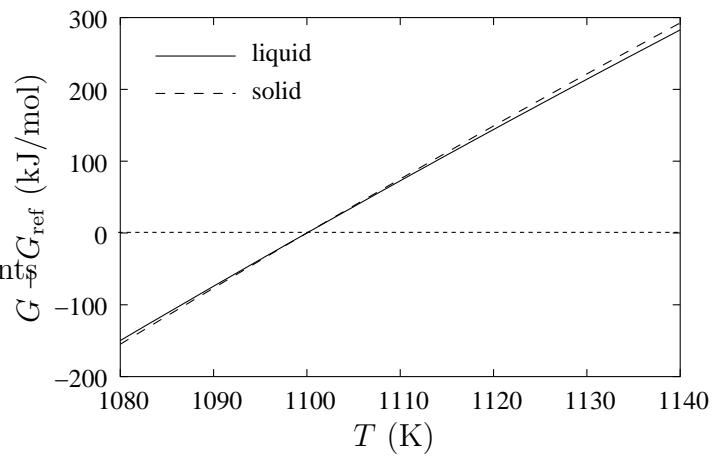


Figure 10: Gibbs free energy (relative to the Gibbs free energy at 1100 K and 1 atm) for both the FCC solid and the liquid phases of EAM Al as a function of temperature.

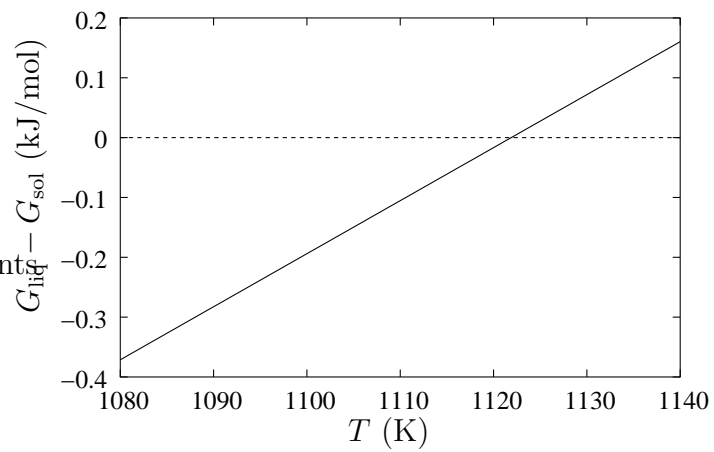


Figure 11: Difference in the Gibbs free energies of the liquid and the solid phases as a function of temperature at 1 atm.

Table 1: Parameters for the embedded atom (EAM) potential.

Constant	Value	Unit
E_c	2.8336616280	eV
ϕ_0	0.209474578	eV
r_0	2.759835989	Å
α	4.953631991	
β	5.202672172	
γ	5.824302949	
δ	8.968682037	
$c(1)$	0.433294196	
$c(2)$	-7.305279256	
$c(3)$	29.818956621	
$c(4)$	-54.437991632	
$c(5)$	48.412067298	
$cc(6)$	-15.525225110	
$s(1)$	6.927645227	
$s(2)$	3.861172975	
$s(3)$	15.498062621	
r_n	$1.75r_0$	Å
r_c	$1.95r_0$	Å

Table 2: Parameters for the explicit many-body (EMB) potential.

Constant	Value	Unit	Constant	Value	Unit
D_e	1.71013678553981441	eV	r_e	5.08182706399609163	Å
a_1	1.24074255007327805	Å ⁻¹	a_2	0.551880801172447422	Å ⁻²
a_3	0.129970688812896917	Å ⁻³	a_{u2}	0.143243771372740580	
b_{u2}	6.5	Å	κ_1	4.24002677622442103	
κ_2	0.117656503960960862		κ_3	4.78063179546451522	
a_{u23}	1.63973192904916298		γ_1	0.708483373073205747	
d	1.13286279334603357		γ	0.663930057862113232	
g_0	8.54498572971970027		γ_2	5.39584023677170066	Å
D'_e	1.42526928794948882	eV	r'_e	4.87735706664722812	Å
a'_1	1.20666644170640880	Å ⁻¹	a'_2	0.728296669115275908	Å ⁻²
a'_3	0.215461507389864804	Å ⁻³	a_{u2b}	0.138211749991007299	
b_{u2b}	6.5	Å			

Table 3: Solid densities and enthalpies for different temperatures.

T (k)	Density (g/cm ³)	Enthalpy (kJ/mol)
300	2.700 ₁	-326.54 ₀
500	2.671 ₁	-323.36 ₁
700	2.632 ₂	-319.86 ₃
900	2.583 ₃	-316.16 ₅
950	2.570 ₁	-315.10 ₁
1000	2.552 ₁	-314.08 ₃
1050	2.540 ₁	-313.07 ₃
1100	2.529 ₁	-312.01 ₂
1150	2.510 ₁	-310.99 ₂
1200	2.500 ₀	-309.96 ₃
1250	2.483 ₂	-308.77 ₃